Tunable Perovskite-Derived Bismuth Halides: $Cs_3Bi_2(Cl_{1-x}I_x)_9$

Emily E. Morgan,[†,‡] Lingling Mao,[*,†] Samuel M. L. Teicher,[†,‡] Guang Wu,[¶] and Ram Seshadri[†,‡,¶]

†*Materials Research Laboratory*

‡*Materials Department*

¶*Department of Chemistry and Biochemistry*

University of California, Santa Barbara, California 93106, United States

E-mail: linglingmao@ucsb.edu

Abstract

Bismuth-based perovskites are of interest as safer alternatives to lead-based optoelectronic materials. Prior studies have reported on the compounds $Cs_3Bi_2Cl_9$, $Cs_3Bi_2I_9$, and $Cs_3Bi_2Cl_3I_6$. Here we examine a range of compounds of the formula $Cs_3Bi_2(Cl_{1-x}I_x)_9$, where x takes values from 0.09 to 0.52. Powder and single crystal X-ray diffraction were used to determine that all of these compounds adopt the layered vacancy-ordered perovskite structure observed for $Cs_3Bi_2Cl_3I_6$, which is also the high-temperature phase of $Cs_3Bi_2Cl_9$. We find that even with very small I incorporation, the structure is switched to that of $Cs_3Bi_2Cl_3I_6$ with I atoms displaying a distinct preference for the capping sites on the BiX_6 octahedra. Optical absorption spectroscopy was employed to study the evolution of optical properties of these materials, and this is complemented by density functional theory electronic structure calculations. Three main absorption features were observed for these compounds, and with increasing x the lowest-energy features are red-shifted.

Introduction

In the past decade, significant improvements have been made in the efficiency of halide perovskite-based solar cells.[1] The most efficient devices have been made using lead-containing perovskites, which have the general chemical formula $A\mathrm{Pb}X_3$, with efficiencies reaching 25.2% for perovskite cells and 28.0% for perovskite-Si tandem cells.[2] Here, A denotes a monovalent cation, which is generally either a large inorganic cation such as Cs^+, or a small organic cation, such as methylammonium or formamidinium, and X denotes a halide, usually Cl^-, Br^-, or I^-. Lead-halide perovskites containing at mixture of different A site cations[3] and X site anions[4] have provided tunability of particular interest to researchers. As these materials now display efficiencies comparable to those seen in commercially-available silicon-based cells, it is likely that they will play a significant role in the future of solar energy.[1]

Despite the promise of lead-halide perovskites, there is substantial concern as to whether they can be implemented on a large scale due to the toxicity associated with lead-based compounds. Although significant lead emissions are already associated with conventional industrial manufacturing and power generation technologies,[5] potentially disastrous levels of lead exposure could occur as a result of the decomposition of lead-perovskite solar cells.[6] While there may be methods to circumvent these issues, many researchers have sought lead-free perovskites that may be able to match the exciting optoelectronic properties associated with lead-halide perovskites. Metals such as tin, germanium, antimony, and bismuth have been proposed as potential substitutes for lead; however, there have not been any reports of lead-free perovskites that have comparable performance to the lead-halide system.[7]

Among these metals, Bi is viewed as one of the most promising alternatives to lead. Bismuth-based perovskites have attracted substantial attention because Bi^{3+} has the same electronic structure as Pb^{2+}, can form the perovskite structure, has low toxicity compared to that of lead, and is air-stable.[8] Accordingly, Bi-based perovskites have been studied

with a variety of combinations of *A*-site cations and *X*-site anion, and in a range of forms, including thin films, nanocrystals, and bulk crystals.[9,10]

Previously, some of us have investigated Bi-based materials such as BiI_3[11] and $A_3Bi_2I_9$ (A = K, Rb, Cs)[12] both experimentally and computationally, and concluded that these materials have properties that make them promising for photovoltaic applications. Furthermore, Park *et al.* proposed the compounds $Cs_3Bi_2I_9$, $MA_3Bi_2I_9$, and $MA_3Bi_2I_{9-x}Cl_x$ as photovoltaic materials with low toxicity, with $Cs_3Bi_2I_9$ exhibiting a power conversion efficiency of greater than 1%.[8] Subsequently, $Cs_3Bi_2I_9$ nanocrystals have been extensively studied for their photovoltaic properties,[13,14] and $MA_3Bi_2I_9$ thin films have achieved improved efficiencies of 3.17%.[15]

While these Bi compounds are bulk 3D crystals, the connectivity of the BiX_6 octahedra often yields an electronic structure with effectively limited dimensionality. In their work, Xiao *et al.* demonstrate that in order for lead-free perovskites to match the efficiencies observed in the *A*PbX_3 compounds, they must exhibit higher electronic dimensionality.[16] Thus, in order to improve the performance of materials such as $Cs_3Bi_2Cl_9$ and $Cs_3Bi_2I_9$, it is of interest to find ways to convert these structures, which feature 1D and 0D connectivity, respectively, to 2D connectivity. One example of this is the compound $Cs_3Bi_2I_6Cl_3$, which has a 2D layered structure, an absorption edge of 2.07 eV, and a direct band gap.[17]

In this work, we expand the family of compounds with the formula $Cs_3Bi_2(Cl_{1-x}I_x)_9$, where x ranges from 0.09 to 0.52 through solution synthesis. The compounds were characterized by X-ray fluorescence spectroscopy, single-crystal and powder X-ray diffraction, UV-vis spectroscopy, and electronic structure calculations, and compared to the end-member compounds. We find that adding small amounts of I to $Cs_3Bi_2Cl_9$ causes a large change in both the structure and electronic properties of the material, and that adding successively greater amounts of I allows systematic tuning of the optical absorption edge within the visible region of the optical spectrum. Interestingly, the structures adopted by members of the solid solution described here are not the stable structures of either of the end-members,

$Cs_3Bi_2Cl_9$ or $Cs_3Bi_2I_9$. Density-functional theory-based electronic structure calculations provide insights into the causes for the dramatic changes in the optical absorption onset upon I substitution.

Experimental

All reagents were purchased from Sigma Aldrich or Fisher Scientific and were used without further purification or modification.

$Cs_3Bi_2Cl_9$ was prepared by adding 1 mmol Bi_2O_3 to 4 cm^3 of HCl (37 wt% in H_2O). The mixture was heated and stirred at 100 °C for 2 min to fully dissolve the Bi_2O_3. 3 mmol CsCl was added to the solution, and the mixture was heated and stirred for an additional 5 min. After cooling, white crystals were isolated and dried by vacuum filtration.

$Cs_3Bi_2I_9$ was prepared by adding 1 mmol Bi_2O_3 to mixture of 4 mL HI (57 wt% in H_2O) and 0.15 cm^3 H_3PO_2 (50 wt% in H_2O). The mixture was heated and stirred at 100 °C for 2 min to fully dissolve the Bi_2O_3. 3 mmol CsCl was added to the solution, and the mixture was heated and stirred for an additional 5 min. After cooling, dark red crystals were isolated and dried by vacuum filtration.

$Cs_3Bi_2Cl_{9-x}I_x$ samples were prepared by first preparing mixtures containing various proportions of HCl (37 wt% in H_2O) and HI (57 wt% in H_2O) by adding volumes of HI varying from 0.05 cm^3 to 0.50 cm^3, to 4 cm^3 HCl. 1 mmol Bi_2O_3 was added to each acid solution. The mixtures were heated and stirred at 100 °C for 2 min to fully dissolve the Bi_2O_3. 3 mmol CsCl was added to each solution, and the mixture were heated and stirred for an additional 15 min. After cooling, crystals which ranged in color from yellow to reddish-orange were isolated and dried by vacuum filtration.

Powder X-ray diffraction (PXRD) measurements were performed on a Panalytical Empyrean powder diffractometer in reflection mode with a Cu-Kα radiation source. Rietveld analysis was performed to estimate lattice parameters using the TOPAS software

package.[18] Single-crystal X-Ray diffraction (SC-XRD) data was collected for $Cs_3Bi_2Cl_9$ and one $Cs_3Bi_2Cl_{9-x}I_x$ sample on a Bruker KAPPA APEX II diffractometer with an APEX II CCD detector, TRIUMPH monochromator, and Mo-Kα radiation source (λ = 0.71073 Å). The crystal structure was solved by direct methods and refined by full-matrix least squares on F2 using the OLEX2 program package.[19] Crystal structures were visualized using the VESTA software package.[20] X-ray fluorescence (XRF) data was collected using a Rigaku ZSX Primus IV XRF spectrometer, which was used to determine the relative mass % of Cl and I present in each sample. The program used was set up to detect Cs, Bi, Cl, and I using the Cs-Kα, Bi-Lα, Cl-Kα, and I-Kα lines with a scanning time of 15 sec and a fixed angle measurement time of 15 sec for each element. Multiple measurements, each with a scan diameter of 0.5 mm, were made for each compound, and the results were averaged to determine the composition of each compound. Absorbance spectra were obtained by measuring diffuse reflectance on a Shimadzu UV3600 UV-Vis-NIR spectrometer equipped with an integrating sphere. Reflectance was converted to absorbance using the Kubelka-Munk transformation.[21]

Density Functional Theory calculations were performed in VASP v5.4.4[22–24] using the PBE[25] and HSE06[26] functionals and PAW pseudopotentials[27,28] with energy convergence better than 10^{-6} eV. PAW potentials were selected based on the version 5.2 recommendations. We used structural parameters from $Cs_3Bi_2Cl_9$ single crystal diffraction for the 0D-connectivity space group 62 structure. For the 2D-connectivity structures in space group 164, we performed calculations using the structure refined from single-crystal X-ray for $Cs_3Bi_2I_{0.8}Cl_{8.2}$ as well as using lattice parameters linearly-interpolated between hypothetical 0% and 100% iodine incorporation structures based on the trends from powder X-ray diffraction Rietveld fits (see Figure 3). We employed a plane-wave energy cut-off of 500 eV and used the automatic k-mesh generation scheme with the length parameter, l, set to 20 and 30 for PBE and HSE06 calculations, respectively ($l = 30$ corresponds to a k-mesh of $4 \times 4 \times 2$ for the group space 62 structure and a mesh between $5 \times 5 \times 3$ and $4 \times 4 \times 3$ for the

group 164 structures). Band structure calculations were performed using a density of 30 and 16 k-points per branch for the PBE and HSE06 calculations, respectively. Using these parameters, the band gaps appear to be converged much better than 0.1 eV in all cases. Crystal orbital Hamilton bonding analysis was performed in LOBSTER.[29–32]

Results and Discussion

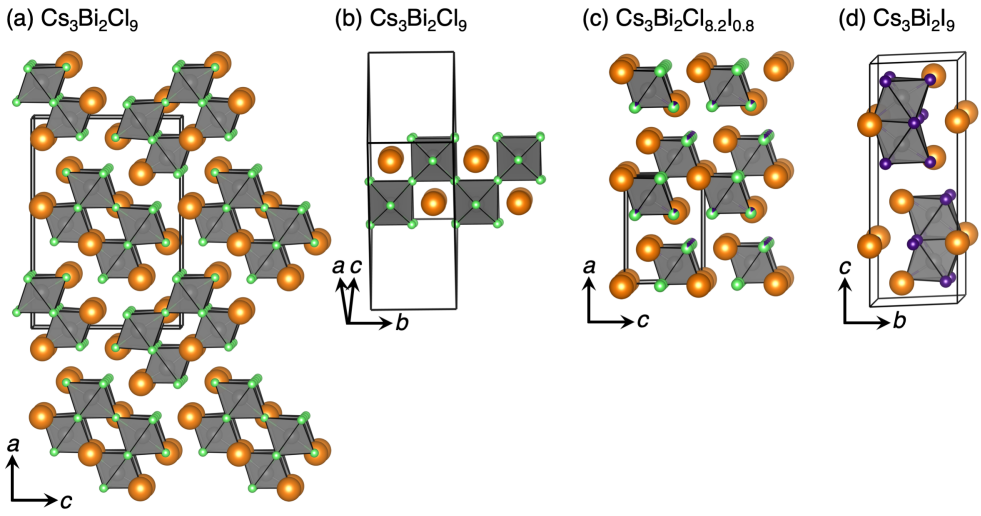

Figure 1: (a) One-dimensional crystal structure of $Cs_3Bi_2Cl_9$ ($Pnma$, S.G. #62) viewed down the 1D chains of $BiCl_6$ octahedra. (b) The same structure of $Cs_3Bi_2Cl_9$ emphasizing one of the chains of $BiCl_6$ octahedra. (c) Two-dimensional vacancy-ordered perovskite structure of $Cs_3Bi_2Cl_{8.16}I_{0.84}$ ($P\bar{3}m1$, S.G. #164) viewed down the b axis, depicting the 2D sheets of $BiCl_6$ octahedra. (d) Zero-dimensional structure of $Cs_3Bi_2I_9$ ($P6_3/mmc$, S.G. #194) showing the condensed, face-shared double octahedra of $Bi_2I_9^{3-}$.

Single crystals of $Cs_3Bi_2Cl_9$ and of a compound whose composition was established to be $Cs_3Bi_2Cl_{8.16}I_{0.84}$ were obtained directly from the reaction mixtures, and their structures as determined from single-crystal X-ray diffraction at room temperature are shown in Figure 1. The conditions for single crystal data collection and select crystallographic pa-

Table 1: Single-crystal X-ray diffraction refinement data and results for two compounds in the series whose crystals structures are depicted.

Empirical formula	$Cs_3Bi_2Cl_9$	$Cs_3Bi_2Cl_{8.16}I_{0.84}$
Form. wt. ($g\,mol^{-1}$)	1135.74	1212.61
Crystal habit and color	Rods, colorless	Hexagonal plates, yellow
Crystal system	Orthorhombic	Trigonal
Space group	$Pnma$ (No. 62)	$P\bar{3}m1$ (No. 164)
Temperature (K)	300	299
Wavelength (Å)	0.71073	0.71073
a (Å)	18.644(5)	7.7587(6)
b (Å)	7.6182(19)	7.7587(6)
c (Å)	13.186(4)	9.5183(8)
α (°)	90	90
α (°)	90	90
γ (°)	90	120
Volume ($Å^3$)	1872.8(8)	496.21(9)
Density (calc.) ($g\,cm^{-3}$)	4.028	4.058
θ range (°)	3.276 to 28.327	2.140 to 30.550
Completeness to θ = 25.242°	99.5%	100%
Reflections collected	8746	3782
Data / restraints / parameters	2497 / 0 / 76	616 / 0 / 20
Goodness-of-fit	1.100	1.097
Final R indices [$I > 2\sigma(I)$]	R_{obs} = 0.0319	R_{obs} = 0.0261
	wR_{obs} = 0.0658	wR_{obs} = 0.0678

rameters are are summarized in Table 1. The structure of $Cs_3Bi_2Cl_9$ matched the reported structure which is found at temperatures up to $T = 646$ K. The structure is orthorhombic, in the $Pnma$ space group and can be visualized as 1D chains of clusters of $BiCl_6$ octahedra (Figure 1 (a,b)). While this structure has corner-connected $BiCl_6$ octahedra reminiscent of perovskite, the disposition of these makes it difficult to relate this structure to perovskite. One test of perovskite with no *A* site vacancies is to check whether the *A* sites describe the topology of a simple cubic lattice. This appears not to be the case for $Cs_3Bi_2Cl_9$.

The compound $Cs_3Bi_2Cl_{8.16}I_{0.84}$ crystalizes in the trigonal space group $P\bar{3}m1$ and adopts a structure than be described by an ordered vacancy (□) ordering on the perovskite $A_3B_2\square X_9$ that results in layers of vacancies separated by double-layers of BiX_6 octahedra. The structure is very similar to that of β-$Cs_3Bi_2Cl_9$, but with a unit cell that is 3.8% smaller than what is reported, potentially due to the thermal expansion of in the structure of β-$Cs_3Bi_2Cl_9$, as it was reported at 723 K.[33] In this structure, the BiX_6 octahedra are corner-sharing and form corrugated 2D layers (Figure 1 (c)). In their characterization of the structure of $Cs_3Bi_2I_6Cl_3$, which has a similar structure, McCall *et.al.* found that the I atoms preferred to occupy the capping positions on the octahedra in the structure, while the Cl atoms occupy the bridging positions between the octahedra.[17] In the refinement of the structure presented here for $Cs_3Bi_2Cl_{8.16}I_{0.84}$, we observe a similar tendency, with corner-sharing sites between octahedra occupied exclusively by Cl, and a mixture of I and Cl atoms in the other sites. This site preference may provide the previously mentioned driving force for the incorporation of I into the structure, as the structure tries to maximize the amount of I in the capping sites. The origin of this site preference is revisited in the discussion of the electronic structure.

The broad family of $A_3B_2\square X_9$ structures have been previously described[34] as adopting 0D, 1D, and 2D variants, based on the order-disorder framework developed by Dornberger-Schiff and Grenn-Niemann.[35] The 2D structures described here are also adopted by $Cs_3Sb_2I_9$[36] and by $Rb_3Bi_2I_9$.[12]

For completion, Figure 1(d) displays the stable crystal structure of $Cs_3Bi_2I_9$ which is again, not perovskite-derived since the BiI_6 form as face-sharing pairs.

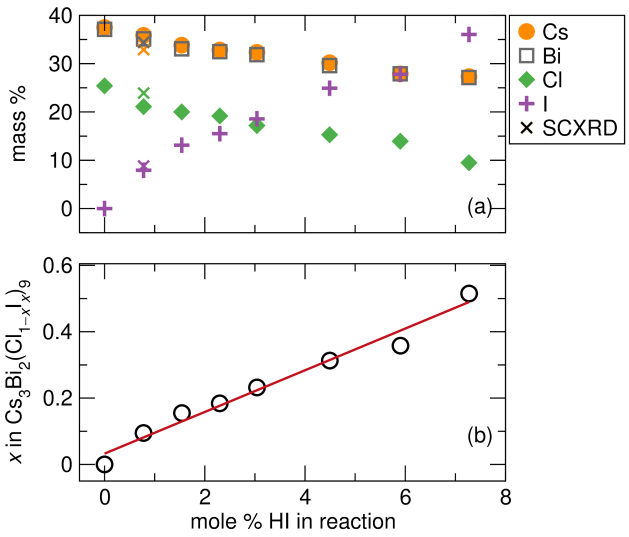

Figure 2: (a) Compositions of the title compounds as determined by X-ray fluorescence (XRF) as a function of the percentage of HI in the reaction mixture. For the solid solution compound $Cs_3Bi_2Cl_{8.16}I_{0.84}$, the composition obtained from single crystal X-ray diffraction (SCXRD) refinement is indicated in appropriate location. (b) I:Cl mass ratios from XRF converted to values of x in $Cs_3Bi_2(Cl_{1-x}I_x)_9$.

The composition of the different $Cs_3Bi_2Cl_{9-x}I_x$ compounds were determined using X-ray fluorescence, and the results are displayed in Figure 2. As expected, it was observed that the mass % of Cl and I vary linearly with the percentage of HI in the reaction mixture. Additionally, it should be noted that in the plot of I occupancy *vs* % HI in the reaction, the slope of the linear fit is close to 6%I/%HI, demonstrating that the occupancy of the *X* sites is not the same as the ratio of I to Cl in the reaction mixture. For example, when the reaction mixture contained 7.27% HI, the product had an I occupancy of 52 %. It is clear from these results that there is a large driving force for the incorporation of I into the structure.

Figure 3 displays the evolution of powder X-ray diffraction patterns of the different compounds in the solid solution that crystallize in the 2D vacancy-ordered perovskite structure in space group $P\bar{3}m1$. The overlaid Rietveld fits suggest that all of the samples are single phase within the detection limits established by laboratory x-ray diffraction data.

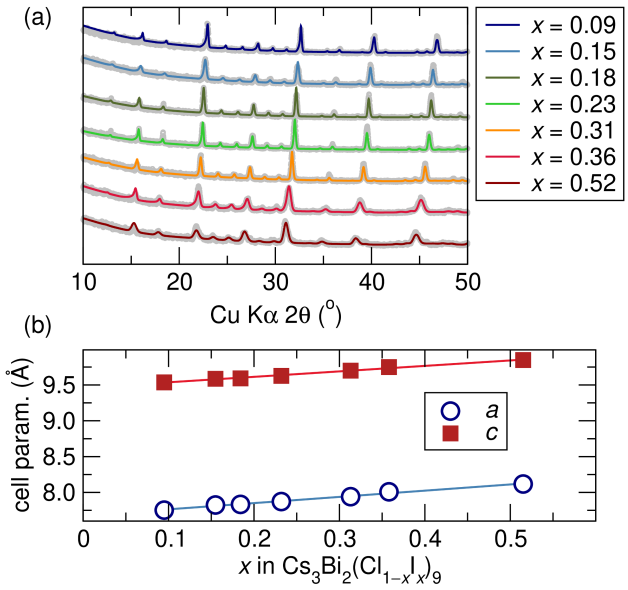

Figure 3: (a) Evolution of X-ray diffraction patterns of the compounds $Cs_3Bi_2(Cl_{1-x}I_x)_9$ with the single-phase Rietveld fits to the 2D vacancy-ordered perovskite structure overlaid. Rietveld analysis confirms the absence of extraneous peaks that would suggest secondary phase. (b) Evolution of the cell parameters with x of $Cs_3Bi_2(Cl_{1-x}I_x)_9$.

In the case of the end-member compounds, powder patterns for $Cs_3Bi_2Cl_9$ and $Cs_3Bi_2I_9$ (not displayed) matched those of previously reported structures for α-$Cs_3Bi_2Cl_9$ and bulk $Cs_3Bi_2I_9$. In addition to a shift to lower 2θ values with increasing I content, the peaks also exhibit broadening with increasing amounts of I, as shown in Figure 3. This broadening is attributed to the decreasing size of the crystallites as the amount of I in the sample increases.

Diffuse reflectance spectra transformed using the Kubelka-Munk method into absorbance for each compound is shown in Figure 4. As expected from the appearance of compounds (shown as an inset), the absorption edge shifts to lower energies with increasing I occupancy. Additionally, the absorbance peak widens with increasing I. From the absorbance data, the absorbance edge for each compound was calculated and is presented as a function of the composition in Figure 4(b). A large decrease in the energy of the first absorption edge is noted immediately upon I incorporation, corresponding to the change from the 1D structure to the 2D structure. As more I is incorporated into the lattice, the

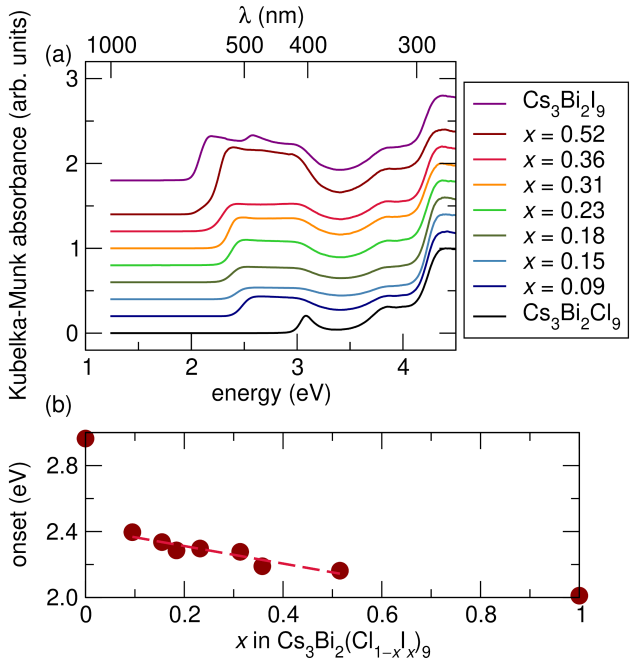

Figure 4: (a) Kubelka-Munk transformed optical absorption data on powders of $Cs_3Bi_2(Cl_{1-x}I_x)_9$. (b) Absorption onset as a function of x. The inset displays a photograph of as-prepared samples of $Cs_3Bi_2(Cl_{1-x}I_x)_9$ in their reactant solution, with x increasing 0.09 to 0.52 from left to right.

energy of the absorption edge decreases nearly linearly with the increasing I occupancy.

Density functional theory-based calculations were carried out in order to gain a better understanding of electronic structure of these new compounds, including the relative roles of roles of structural connectivity and I substitution on the measured band gaps. Figure 5 presents the calculated band gaps of compounds with the vacancy-ordered perovskite structure. This includes hypothetical compounds with compositions of $Cs_3Bi_2Cl_9$, $Cs_3Bi_2I_9$, $Cs_3Bi_2Cl_3I_6$, in which I sits on the $6i$ capping Wyckoff site and Cl sits on the $3e$ site, and $Cs_3Bi_2Cl_6I_3$, in which Cl and I occupation is reversed to the $6i$ and $3e$ sites, respectively. The treatment of these four structures provides qualitative understanding of the role of I site occupation without breaking space group symmetry and needing to consider more complex supercell calculations. In addition to stoichiometric changes, there is significant lattice expansion with increased I concentration. In order to account this effect, we have repeated calculations for all four structures at lattice parameters corresponding to 0 %,

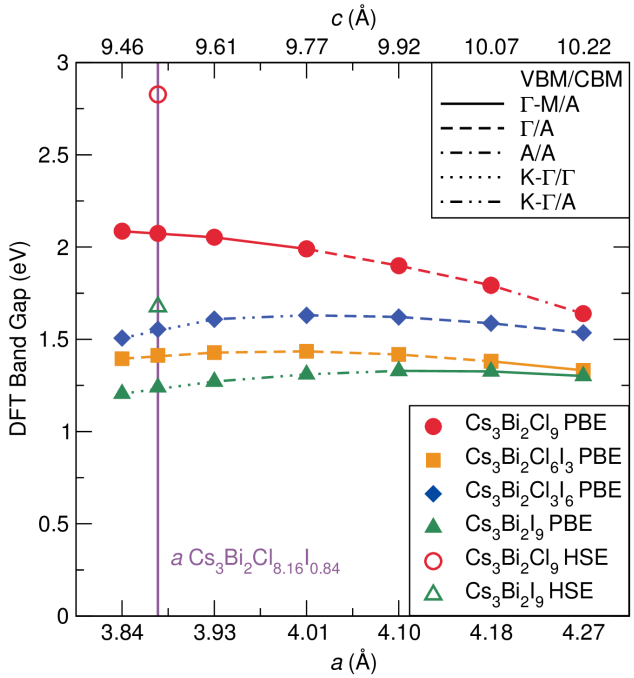

Figure 5: DFT band gaps of compounds in the vacancy-ordered 2D perovskite structure in space group $P\bar{3}m1$. We compare simulations of compounds $Cs_3Bi_2Cl_9$, $Cs_3Bi_2Cl_6I_3$, $Cs_3Bi_2Cl_3I_6$, and $Cs_3Bi_2I_9$ structures with varying iodine filling and varying lattice parameter. In addition, we have repeated all the calculations using the lattice parameters of $Cs_3Bi_2Cl_{8.16}I_{0.84}$ determined by single crystal X-ray diffraction (Note: the c/a ratio for $Cs_3Bi_2Cl_{8.16}I_{0.84}$ is slightly different from that determined by powder Rietveld refinement, so the c axis is not valid for these data points; the adjustment is very minor, however). All simulations incorporated spin-orbit coupling.

20 %, 40 %, 60 %, 80 %, and 100 % I substitution based on the linear lattice parameter trends of the powder Rietveld fits (Figure 3) as well as the lattice parameters of single crystal $Cs_3Bi_2Cl_{8.16}I_{0.84}$.

Transitions of the valence band maximum (VBM) and conduction band minimum (CBM) in Figure 5 are displayed using dashed lines. We find that across this solid solution, as in other perovskite systems with relatively flat conduction bands,[37] a great number of direct and indirect transitions can be favored based on subtle changes in bonding. Second, the fact that both $Cs_3Bi_2Cl_9$ and $Cs_3Bi_2I_9$ in the vacancy-ordered perovskite structure adopts a Γ-M/A gap in at their preferred lattice parameters suggests that the dominant transitions in the real material should be close to Γ-M/A.

When comparing with the calculated bandgap (PBE) for the 1D chain ($Pnma$) structure of $Cs_3Bi_2Cl_9$ structure of 2.32 eV (Figure 6), the band gap of $Cs_3Bi_2Cl_9$ in the hypothetical 0% Cl $P\bar{3}m1$ structure is 2.09 eV, which is smaller, but not significantly so. Comparing with the large optical absorption onset energy decrease between the first two data points of Figure 4(b) (≈ 0.5 eV) suggests that structural transformation to the 2D-connectivity alone is not sufficient to recreate the band gap trend. The lattice parameter trend alone also appears insufficient to explain the large reduction in the experimental band gap. While the bandgap of $Cs_3Bi_2Cl_9$ decreases by about 0.3 eV upon compression to the $Cs_3Bi_2I_9$ structure, the trend is reversed for any of the structures with I. The full I structure has a much smaller band gap than that of the full Cl structure and the magnitude of this reduction is consistent with the large drop seen in experiment. This is not surprising because of the relatively large size of I orbitals compared to Cl orbitals and the expectation that there will therefore be larger band dispersion in the I compound. The HSE band gaps, which are expected to quantitatively match the measured values more closely than the PBE values, further confirm this intuition. The HSE band gap of the full Cl compound is quite close to that of $Cs_3Bi_2Cl_9$ measured in experiment, and the 2.8 ev to 1.7 eV band gap range between Cl and I compounds is roughly consistent with the range seen in experiment,

albeit downshifted by about 0.2 eV from the values of 4(b).

A more subtle point is that the band gap of $Cs_3Bi_2Cl_6I_3$ is systematically lower than that of $Cs_3Bi_2Cl_3I_6$. This may seem surprising at first because the latter structure has double the concentration of I. This is due to the different bond distances and bond strengths for $6i$ and $3e$ site occupancy. The value of the integrated crystal orbital Hamilton population (ICOHP) has been found to form an effective computational proxy for bond strength in a wide variety of systems. The more negative the ICOHP, the stronger the bonding. Larger ICOHPs evidence stronger bonding in the full I structures: -3.4 eV and -2.1 eV for Bi-I bonding in $Cs_3Bi_2I_9$ on $6i$ and $3e$ sites, respectively, while for Bi–Cl bonding in $Cs_3Bi_2I_9$ on the same sites these values are -2.5 eV and -1.5 eV (here, we consider the ICOHP in the single crystal structure of $Cs_3Bi_2Cl_{8.16}I_{0.84}$. Moreover, the bonding strength of I on the $6i$ capping site is much greater than I on the $3e$ site or Cl on either site; this may explain the strong preference for I occupation on the $6i$ site. The bonding asymmetry is more broadly reflective of asymmetry in the electron distribution near the Bismuth atom. The inset of Figure 6 shows the electron localization function of the Bi atom in relation to the octahedral bonding demonstrating a stereochemically-active lone pair that points away from the $6i$ sites and towards the $3e$ sites.

Figure 6 shows selected portions of the orbital-projected band structures of $Cs_3Bi_2Cl_9$ in the 2D vacancy-ordered perovskite structure ($P\bar{3}m1$) and the structure with 1D chains ($Pnma$). As expected, the 2D-bonding connectivity structure can be seen to have larger band dispersions in both the conduction and valence band than the 1D-connectivity $Pnma$ structure. As in many other perovskite systems, electron filling of the Cl/I p orbitals and the loss of electrons by Bi p yields a band structure with dominant Cl/I p contributions in the valence band and dominant Bi p in the conduction band. A large Bi s contribution at the top of the valence band arises due to Bi s / Cl p antibonding interactions. The third panel of Figure 6 presents the un-integrated partial COHP of Bi–Cl bonding interactions in the 2D $P\bar{3}m1$ structure. Atoms on both the $6i$ and $3e$ sites contribute to the Bi s / Cl

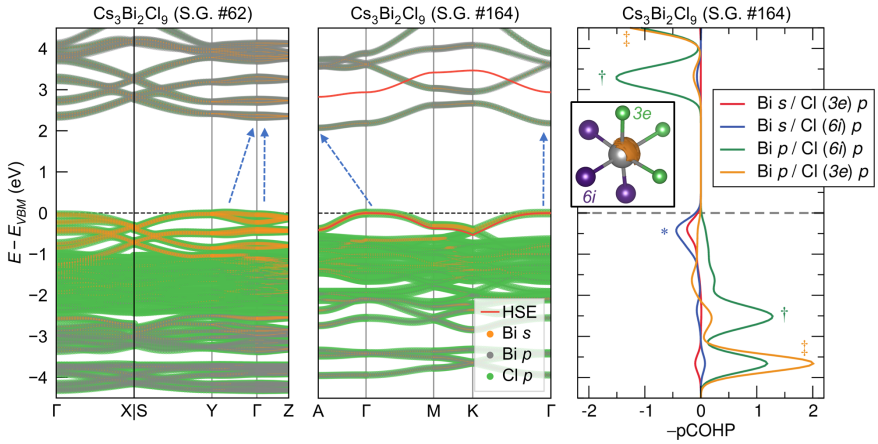

Figure 6: Calculated band structures of $Cs_3Bi_2Cl_9$ in the 1D chain structure ($Pnma$, S.G. 62) of $Cs_3Bi_2Cl_9$ and 2D vacancy-ordered perovskite structure ($P\bar{3}m1$, S.G. 164) of $Cs_3Bi_2Cl_{8.16}I_{0.84}$ single-crystal refined structures. The size of the dots represents the relative magnitude of orbital projections. Blue arrows indicate the smallest direct and indirect bandgaps (Γ/Γ;Γ-Y/Γ for the $Pnma$ structure and Γ/Γ;Γ-M/A for the $P\bar{3}m1$ structure). The HSE conduction and valence band are provided for reference on the S.G. 164 band structure. The third panel shows bond-projected COHP pairs for Bi–Cl orbital bonding with Cl on the $3e$ and $6i$ octahedral sites. The inset shows the electron localization function on the Bi atom at a contour of 0.57 electron in relation to the $3e$ and $6i$ sites. Annotations indicate: ($*$) Bi-s/Cl-p antibonding contribution at the VBM, (†) Bi-p-Cl($6i$)-p bonding and antibonding states that contribute to the CBM, and (‡) Bi-p-Cl($3e$)-p bonding and antibonding states that contribute to neither the CBM nor the VBM.

p antibonding interactions($*$) that push the VBM upwards in energy, whereas only atoms on the $6i$ site contribute to the Bi p / Cl p antibonding interaction(†) that pushes the CBM upwards in energy. This explains why the band gap of $Cs_3Bi_2Cl_6I_3$ is lower than that of $Cs_3Bi_2Cl_3I_6$. While placing I on either site increases bonding strength and band dispersion, ultimately closing the band gap, placing I on the non-preferred $3e$ site raises the energy of the Bi s/Cl p antibonding states in the valence band without also raising the energy of antibonding Bi p/Cl p states in the conduction band, closing the band gap much more rapidly.

Overall, the computational results suggests that, in addition to the increased 2D bonding connectivity in the vacancy-ordered perovskite structures, the effect of I incorporation on local bonding is essential to explaining the sharp reduction in band gap seen in experiment. Bonding asymmetry due to the stereochemically-active lone pair on the Bi is likely one reason for the preference for I occupation on the capping sites.

Conclusion

We have shown that even small I incorporation (small x) in the solid solution $Cs_3Bi_2(Cl_{1-x}I_x)_9$ switches the structure to the vacancy-ordered perovskite-type in the trigonal space group $P\bar{3}m1$. Associated with this substitution are dramatic changes in the optical properties, which can be further tuned with increasing I incorporation. Density functional theory-based electronic structure calculations point to the importance of the electronic changes induced by the orbital states of I over the changes in the structural dimensionality as dominating the changes in the optical absorption properties. They also point to the potential origin of the site-preference tendency of I^- that results in the structure being switched from 1D to perovskite-derived 2D upon I^- incorporation.

Supporting Information

X-ray crystallographic data for $Cs_3Bi_2Cl_9$ and $Cs_3Bi_2Cl_{8.16}I_{0.84}$ (CIF), optical microscopic images (Figure S1) additional crystallographic data (Tables S1 to S6), Rietveld fit depictions for all of the samples (Figures S2 to S8) and computational data including (Tables S7 to S10) (PDF).

Acknowledgments

This work was supported by the U.S. Department of Energy, Office of Science, Basic Energy Sciences under award number DE-SC-0012541. Use of the Shared Experimental Facilities of the Materials Research Science and Engineering Center (MRSEC) at UCSB (NSF DMR 1720256) is gratefully acknowledged. The UCSB MRSEC is a member of the NSF-supported Materials Research Facilities Network (www.mrfn.org). We additionally acknowledge support from the Center for Scientific Computing at UCSB, supported by the NSF CNS-1725797 and NSF DMR-1720256. SMLT has been supported by the National Science Foundation Graduate Research Fellowship Program under Grant No. DGE-1650114. Any opinions, findings, and conclusions or recommendations expressed in this material are those of the authors and do not necessarily reflect the views of the National Science Foundation.

References

(1) Snaith, H. J. Present Status and Future Prospects of Perovskite Photovoltaics. *Nat. Mater.* **2018**, *17*, 372–376, DOI: 10.1038/s41563-018-0071-z.

(2) National Renewable Energy Laboratory, Best Research-Cell Efficiency Chart. https://www.nrel.gov/pv/cell-efficiency.html.

(3) Saparov, B.; Mitzi, D. B. Organic-Inorganic Perovskites: Structural Versatility for Functional Materials Design. *Chem. Rev.* **2016**, *116*, 4558–4596, DOI: 10.1021/acs.chemrev.5b00715.

(4) Wang, H.; Bian, H.; Jin, Z.; Zhang, H.; Liang, L.; Wen, J.; Wang, Q.; Ding, L.; Liu, S. F. Cesium Lead Mixed-Halide Perovskites for Low Energy Loss Solar Cells with Efficiency Beyond 17%. *Chem. Mater.* **2019**, DOI: 10.1021/acs.chemmater.9b02248.

(5) Fabini, D. Quantifying the Potential for Lead Pollution from Halide Perovskite Photovoltaics. *J. Phys. Chem. Lett.* **2015**, *6*, 3546–3548, DOI: 10.1021/acs.jpclett.5b01747.

(6) Babayigit, A.; Ethirajan, A.; Muller, M.; Conings, B. Toxicity of Organometal Halide Perovskite Solar Cells. *Nat. Mater.* **2016**, *15*, 247–251, DOI: 10.1038/nmat4572.

(7) Shi, Z.; Guo, J.; Chen, Y.; Li, Q.; Pan, Y.; Zhang, H.; Xia, Y.; Huang, W. Lead-Free Organic–Inorganic Hybrid Perovskites for Photovoltaic Applications: Recent Advances and Perspectives. *Adv. Mater.* **2017**, *29*, 1605005, DOI: 10.1002/adma.201605005.

(8) Park, B.-W.; Philippe, B.; Zhang, X.; Rensmo, H.; Boschloo, G.; Johansson, E. M. Bismuth Based Hybrid Perovskites $A_3Bi_2I_9$ (*A*: Methylammonium or Cesium) for Solar Cell Application. *Adv. Mater.* **2015**, *27*, 6806–6813, DOI: 10.1002/adma.201501978.

(9) Abulikemu, M.; Ould-Chikh, S.; Miao, X.; Alarousu, E.; Murali, B.; Ndjawa, G. O. N.; Barbé, J.; El Labban, A.; Amassian, A.; Del Gobbo, S. Optoelectronic and Photovoltaic

Properties of the Air-Stable Organohalide Semiconductor $(CH_3NH_3)_3Bi_2I_9$. *J. Mater. Chem. A* **2016**, *4*, 12504–12515, DOI: 10.1039/C6TA04657F.

(10) Creutz, S. E.; Liu, H.; Kaiser, M. E.; Li, X.; Gamelin, D. R. Structural Diversity in Cesium-Bismuth-Halide Nanocrystals. *Chem. Mater.* **2019**, *31*, 4685–4697, DOI: 10.1021/acs.chemmater.9b00640.

(11) Lehner, A. J.; Wang, H.; Fabini, D. H.; Liman, C. D.; Hébert, C.-A.; Perry, E. E.; Wang, M.; Bazan, G. C.; Chabinyc, M. L.; Seshadri, R. Electronic Structure and Photovoltaic Application of BiI_3. *Appl. Phys. Lett.* **2015**, *107*, 131109, DOI: 10.1063/1.4932129.

(12) Lehner, A. J.; Fabini, D. H.; Evans, H. A.; Hébert, C.-A.; Smock, S. R.; Hu, J.; Wang, H.; Zwanziger, J. W.; Chabinyc, M. L.; Seshadri, R. Crystal and Electronic Structures of Complex Bismuth Iodides $A_3Bi_2I_9$ (A = K, Rb, Cs) Related to Perovskite: Aiding the Rational Design of Photovoltaics. *Chem. Mater.* **2015**, *27*, 7137–7148, DOI: 10.1021/acs.chemmater.5b03147.

(13) Lou, Y.; Fang, M.; Chen, J.; Zhao, Y. Formation of Highly Luminescent Cesium Bismuth Halide Perovskite Quantum Dots Tuned by Anion Exchange. *Chem. Comm.* **2018**, *54*, 3779–3782, DOI: 10.1039/C8CC01110A.

(14) Leng, M. et al. All-Inorganic Bismuth-Based Perovskite Quantum Dots with Bright Blue Photoluminescence and Excellent Stability. *Adv. Funct. Mater.* **2018**, *28*, 1704446, DOI: 10.1002/adfm.201704446.

(15) Jain, S. M.; Phuyal, D.; Davies, M. L.; Li, M.; Philippe, B.; De Castro, C.; Qiu, Z.; Kim, J.; Watson, T.; Tsoi, W. C.; Karis, O.; Rensmo, H.; Boschloo, G.; Edvinsson, T.; Durrant, J. R. An Effective Approach of Vapour Assisted Morphological Tailoring for Reducing Metal Defect Sites in Lead-Free, $(CH_3NH_3)_3Bi_2I_9$ Bismuth-Based Perovskite

Solar Cells for Improved Performance and Long-Term Stability. *Nano Energy* **2018**, *49*, 614–624, DOI: 10.1016/j.nanoen.2018.05.003.

(16) Xiao, Z.; Meng, W.; Wang, J.; Mitzi, D. B.; Yan, Y. Searching for Promising New Perovskite-Based Photovoltaic Absorbers: the Importance of Electronic Dimensionality. *Mater. Horiz.* **2017**, *4*, 206–216, DOI: 10.1039/C6MH00519E.

(17) McCall, K. M.; Stoumpos, C. C.; Kontsevoi, O. Y.; Alexander, G. C.; Wessels, B. W.; Kanatzidis, M. G. From 0D $Cs_3Bi_2I_9$ to 2D $Cs_3Bi_2I_6Cl_3$: Dimensional Expansion Induces a Direct Band Gap but Enhances Electron–Phonon Coupling. *Chem. Mater.* **2019**, *31*, 2644–2650, DOI: 10.1021/acs.chemmater.9b00636.

(18) Coelho, A. A. TOPAS and TOPAS-Academic: An Optimization Program Integrating Computer Algebra and Crystallographic Objects Written in C++. *J. Appl. Crystallogr.* **2018**, *51*, 210–218, DOI: 10.1107/S1600576718000183.

(19) Dolomanov, O. V.; Bourhis, L. J.; Gildea, R. J.; Howard, J. A. K.; Puschmann, H. OLEX2: A Complete Structure Solution, Refinement and Analysis Program. *J. Appl. Crystallogr.* **2009**, *42*, 339–341, DOI: 10.1107/S0021889808042726.

(20) Momma, K.; Izumi, F. VESTA 3 for Three-Dimensional Visualization of Crystal, Volumetric and Morphology Data. *J. Appl. Crystallogr.* **2011**, *44*, 1272–1276, DOI: 10.1107/S0021889811038970.

(21) Kubelka, P. Ein Beitrag zur Optik der Farbanstriche. *Z. Phys.* **1931**, *12*, 593–601.

(22) Kresse, G.; Hafner, J. Ab Initio Molecular-Dynamics Simulation of the Liquid-Metal–Amorphous-Semiconductor Transition in Germanium. *Phys. Rev. B* **1994**, *49*, 14251, DOI: 10.1103/PhysRevB.49.14251.

(23) Kresse, G.; Furthmüller, J. Efficient Iterative Schemes for Ab Initio Total-Energy

Calculations Using a Plane-Wave Basis Set. *Phys. Rev. B* **1996**, *54*, 11169, DOI: 10.1103/PhysRevB.54.11169.

(24) Kresse, G.; Furthmüller, J. Efficiency of ab-initio Total Energy Calculations for Metals and Semiconductors Using a Plane-Wave Basis Set. *Comput. Mater. Sci.* **1996**, *6*, 15, DOI: 10.1016/0927-0256(96)00008-0.

(25) Perdew, J. P.; Burke, K.; Ernzerhof, M. Generalized Gradient Approximation Made Simple. *Phys. Rev. Lett.* **1996**, *77*, 3865, DOI: 10.1103/PhysRevLett.77.3865.

(26) Heyd, J.; Scuseria, G. E.; Ernzerhof, M. Erratum: "Hybrid functionals based on a screened Coulomb potential" [J. Chem. Phys. 118, 8207 (2003)]. *J. Chem. Phys.* **2006**, *124*, 219906, DOI: 10.1063/1.2204597.

(27) Blöchl, P. E. Projector Augmented-Wave Method. *Phys. Rev. B* **1994**, *50*, 17953, DOI: 10.1103/PhysRevB.50.17953.

(28) Kresse, G.; Joubert, D. From Ultrasoft Pseudopotentials to the Projector Augmented-Wave Method. *Phys. Rev. B* **1999**, *59*, 1758, DOI: 10.1103/PhysRevB.59.1758.

(29) Dronskowski, R.; Bloechl, P. E. Crystal Orbital Hamilton populations (COHP): Energy-Resolved Visualization of Chemical Bonding in Solids Based on Density-Functional Calculations. *J. Phys. Chem.* **1993**, *97*, 8617, DOI: 10.1021/j100135a014.

(30) Deringer, V. L.; Tchougréeff, A. L.; Dronskowski, R. Crystal Orbital Hamilton Population (COHP) Analysis As Projected from Plane-Wave Basis Sets. *J. Phys. Chem. A* **2011**, *115*, 5461, DOI: 10.1021/jp202489s.

(31) Maintz, S.; Deringer, V. L.; Tchougréeff, A. L.; Dronskowski, R. Analytic Projection from Plane-Wave and PAW Wavefunctions and Application to Chemical-Bonding Analysis in Solids. *J. Comput. Chem.* **2013**, *34*, 2557, DOI: 10.1002/jcc.23424.

(32) Maintz, S.; Deringer, V. L.; Tchougréeff, A. L.; Dronskowski, R. LOBSTER: A Tool to Extract Chemical Bonding from Plane-Wave Based DFT. *J. Comput. Chem.* **2016**, *37*, 1030, DOI: 10.1002/jcc.24300.

(33) Meyer, G.; Schönemund, A. Zur Kenntnis der Hochtemperatur-Phasenumwandlug bei $Cs_3Bi_2Cl_9$. *Z. Anor. Allg. Chem.* **1980**, *468*, 185–192, DOI: 10.1002/zaac.19804680123.

(34) Arakcheeva, A.; Novikova, M.; Zaitsev, A.; Lubman, G. Perovskite-like Modification of $Cs_3Sb_2I_9$ as a Member of the OD family $A_3B_2X_9$. *J. Struct. Chem.* **1999**, *40*, 572–579.

(35) Dornberger-Schiff, K.; Grell-Niemann, H. On the Theory of Order–Disorder (OD) Structures. *Acta Crystallogr.* **1961**, *14*, 167–177.

(36) Benachenhou, F.; Mairesse, G.; Nowogrocki, G.; Thomas, D. Structural Studies of Cs–K–Bi Mixed Chlorides Relation to the Crystal Structures of A_2BMX_6, A_3MX_6, and A_2MX_6. *J. Solid State Chem.* **1986**, *65*, 13–26.

(37) Mao, L.; Teicher, S. M. L.; Stoumpos, C. C.; Kennard, R. M.; DeCrescent, R. A.; Wu, G.; Schuller, J. A.; Chabinyc, M. L.; Cheetham, A. K.; Seshadri, R. Chemical and Structural Diversity of Hybrid Layered Double Perovskite Halides. *J. Am. Chem. Soc.* **2019**, DOI: 10.1021/jacs.9b09945.

For Table of Contents

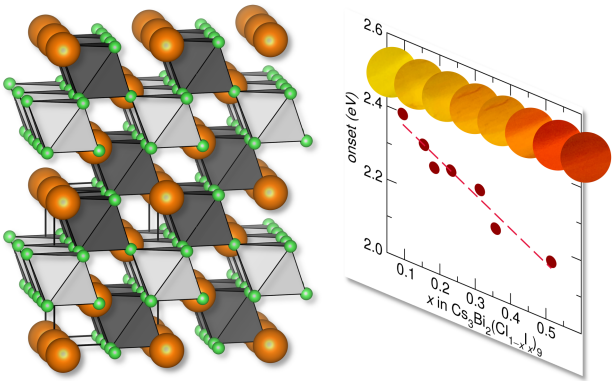

Layered variant of the vacancy-ordered perovskite $A_3B_2\square X_9$ crystal structure with light and dark octahedra respectively depicting vacant $\square X_6$ and filled BX_6. Intermediate compositions of the solid solution $Cs_3Bi_2(Cl_{1-x}I_x)_9$ adopt this structure and increasing iodine incorporation (increasing x) red-shifts the optical absorption onset.

Supporting information for

Tunable Perovskite-Derived Bismuth Halides: $Cs_3Bi_2(Cl_{1-x}I_x)_9$

Emily E. Morgan,[1,2] Lingling Mao,[1,*] Samuel M. L. Teicher ,[1,2] Guang Wu[3], and Ram Seshadri[1,2,3]

[1]Materials Research Laboratory

[2]Materials Department

[3]Department of Chemistry and Biochemistry

University of California, Santa Barbara, California 93106, United States

*Email: linglingmao@ucsb.edu

Table of contents

Section S1. Additional crystallographic details

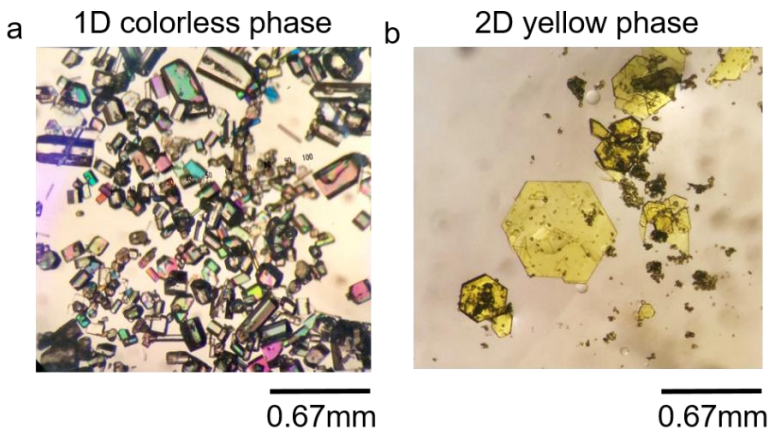

Figure S1. Optical microscopic images of the 1D colorless phase and 2D yellow phase of $Cs_3Bi_2Cl_9$ and $Cs_3Bi_2Cl_{8.16}I_{0.84}$.

Table S1. Atomic coordinates ($\times 10^4$) and equivalent isotropic displacement parameters ($Å^2 \times 10^3$) for $Cs_3Bi_2Cl_9$ with estimated standard deviations in parentheses.

Label	*x*	*y*	*z*	Occupancy	U_{eq}*
Bi(01)	6833(1)	7500	4179(1)	1	18(1)
Bi(02)	4988(1)	2500	2363(1)	1	19(1)
Cs(03)	9112(1)	12500	5811(1)	1	40(1)
Cs(04)	7518(1)	2500	2521(1)	1	42(1)
Cs(05)	9135(1)	7500	892(1)	1	44(1)
Cl(06)	4200(1)	77(2)	1633(2)	1	43(1)
Cl(07)	5885(2)	5032(2)	3321(2)	1	53(1)
Cl(08)	5797(2)	2500	820(2)	1	45(1)
Cl(09)	7511(1)	10043(2)	5037(2)	1	41(1)
Cl(0A)	7539(2)	7500	2503(2)	1	42(1)
Cl(0B)	5873(2)	7500	5833(2)	1	50(1)

*U_{eq} is defined as one third of the trace of the orthogonalized U_{ij} tensor.

Table S2. Atomic coordinates (×10⁴) and equivalent isotropic displacement parameters (Å²×10³) for $Cs_3Bi_2Cl_{8.16}I_{0.84}$ with estimated standard deviations in parentheses.

Label	*x*	*y*	*z*	Occupancy	U_{eq}*
Bi	6666.67	3333.33	8161(1)	1	23(1)
Cs(1)	3333.33	6666.67	6661(2)	1	58(1)
Cs(2)	0	0	0	1	71(1)
Cl(1)	3327(3)	1664(2)	6626(2)	0.861(5)	64(1)
I(1)	3327(3)	1664(2)	6626(2)	0.139(5)	64(1)
Cl(2)	5000	5000	0	1	71(2)

*U_{eq} is defined as one third of the trace of the orthogonalized U_{ij} tensor.

Table S3. Anisotropic displacement parameters (Å² × 10³) for $Cs_3Bi_2Cl_9$ with estimated standard deviations in parentheses.

Label	U_{11}	U_{22}	U_{33}	U_{12}	U_{13}	U_{23}
Bi(01)	19(1)	19(1)	15(1)	0	0(1)	0
Bi(02)	18(1)	21(1)	18(1)	0	0(1)	0
Cs(03)	45(1)	44(1)	32(1)	0	1(1)	0
Cs(04)	38(1)	46(1)	43(1)	0	8(1)	0
Cs(05)	45(1)	40(1)	46(1)	0	−1(1)	0
Cl(06)	47(1)	39(1)	44(1)	−17(1)	−9(1)	−8(1)
Cl(07)	52(2)	46(1)	60(2)	−21(1)	−13(2)	−15(1)
Cl(08)	46(2)	58(2)	32(2)	0	20(2)	0
Cl(09)	40(1)	36(1)	46(1)	−11(1)	−7(1)	−12(1)
Cl(0A)	40(2)	57(2)	27(2)	0	17(1)	0
Cl(0B)	50(2)	66(2)	34(2)	0	23(2)	0

The anisotropic displacement factor exponent takes the form: $-2\pi^2[h^2a^{*2}U_{11} + \ldots + 2hka^*b^*U_{12}]$.

Table S4. Anisotropic displacement parameters ($Å^2 \times 10^3$) for $Cs_3Bi_2Cl_{8.16}I_{0.84}$ with estimated standard deviations in parentheses.

Label	U_{11}	U_{22}	U_{33}	U_{12}	U_{13}	U_{23}
Bi	25(1)	25(1)	19(1)	13(1)	0	0
Cs(1)	64(1)	64(1)	46(1)	32(1)	0	0
Cs(2)	57(1)	57(1)	99(2)	28(1)	0	0
Cl(1)	70(2)	69(1)	53(1)	35(1)	-12(1)	-6(1)
I(1)	70(2)	69(1)	53(1)	35(1)	-12(1)	-6(1)
Cl(2)	84(2)	84(2)	69(2)	60(2)	18(1)	-18(1)

The anisotropic displacement factor exponent takes the form: $-2\pi^2[h^2a^{*2}U_{11} + \ldots + 2hka^*b^*U_{12}]$.

Table S5. Selected bond lengths [Å] for $Cs_3Bi_2Cl_9$ with estimated standard deviations in parentheses.

Label	Distances
Bi(01)-Cl(07)#3	2.8180(17)
Bi(01)-Cl(07)	2.8181(17)
Bi(01)-Cl(09)	2.5748(17)
Bi(01)-Cl(09)#3	2.5748(17)
Bi(01)-Cl(0A)	2.572(2)
Bi(01)-Cl(0B)	2.823(3)
Bi(02)-Cl(06)	2.5475(16)
Bi(02)-Cl(06)#8	2.5475(16)
Bi(02)-Cl(07)#8	2.8487(17)
Bi(02)-Cl(07)	2.8487(17)
Bi(02)-Cl(08)	2.532(2)
Bi(02)-Cl(0B)#9	2.870(3)

Symmetry transformations used to generate equivalent atoms:

(1) x,y+1,z (2) -x+3/2,-y+1,z+1/2 (3) x,-y+3/2,z (4) -x+3/2,-y+2,z-1/2 (5) x-1/2,y-1,-z+1/2 (6) -x+3/2,-y+1,z-1/2 (7) x-1/2,y,-z+1/2 (8) x,-y+1/2,z (9) -x+1,-y+1,-z+1 (10) -x+3/2,y+3/2,z+1/2 (11) x+1/2,-y+3/2,-z+1/2 (12) x+1/2,y+1,-z+1/2 (13) -x+3/2,y+1/2,z+1/2 (14) -x+3/2,-y+2,z+1/2 (15) x,-y+5/2,z (16) x+1/2,y,-z+1/2 (17) x+1/2,-y+1/2,-z+1/2 (18) x,y-1,z (19) -x+3/2,y-1/2,z-1/2 (20) -x+3/2,y+1/2,z-1/2

Table S6. Bond lengths [Å] for $Cs_3Bi_2Cl_{8.16}I_{0.84}$ with estimated standard deviations in parentheses.

Label	Distances
Bi(01)-Cl(1)#1	2.6772(19)
Bi(01)-Cl(2)#1	2.8428(2)

Symmetry transformations used to generate equivalent atoms:

(1) -y+1,x-y,z (2) -x+y+1,-x+1,z (3) y,-x+y+1,-z+1 (4) x-y,x,-z+1 (5) -x+1,-y+1,-z+1 (6) -y,x-y,z (7) x,y+1,z (8) x-1,y-1,z (9) -x+y,-x+1,z (10) -x+y,-x,z (11) x,y-1,z (12) -x+1,-y+1,-z+2 (13) x+1,y+1,z

Section S2. Rietveld analysis of $Cs_3Bi_2(Cl_{1-x}I_x)_9$ compounds

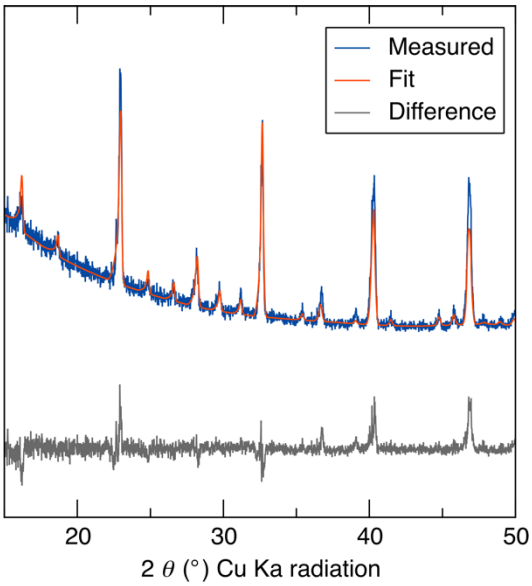

Figure S2. Rietveld refinement for compound with *x*=0.095 showing the PXRD data, the Rietveld fit produced by TOPAS, and the difference between them.

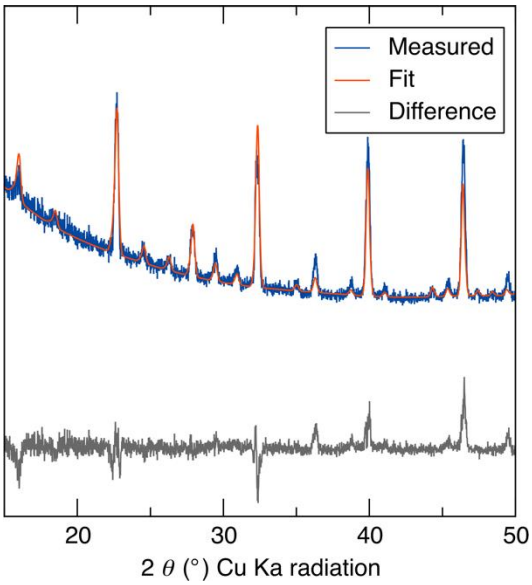

Figure S3. Rietveld refinement for compound with *x*=0.16 showing the PXRD data, the Rietveld fit produced by TOPAS, and the difference between them.

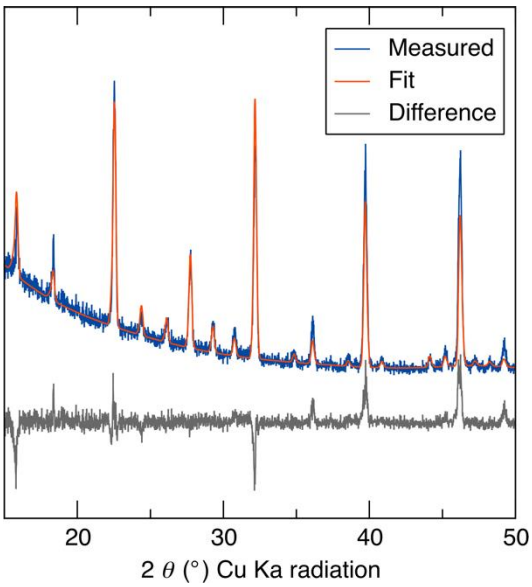

Figure S4. Rietveld refinement for compound with *x*=0.18 showing the PXRD data, the Rietveld fit produced by TOPAS, and the difference between them.

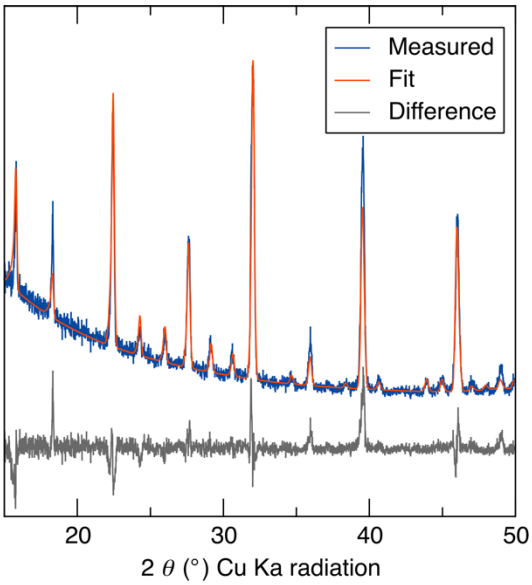

Figure S5. Rietveld refinement for compound with *x*=0.23 showing the PXRD data, the Rietveld fit produced by TOPAS, and the difference between them.

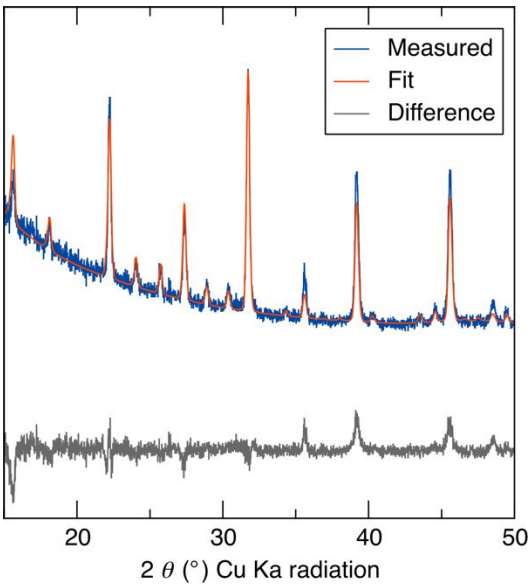

Figure S6. Rietveld refinement for compound with *x*=0.31 showing the PXRD data, the Rietveld fit produced by TOPAS, and the difference between them.

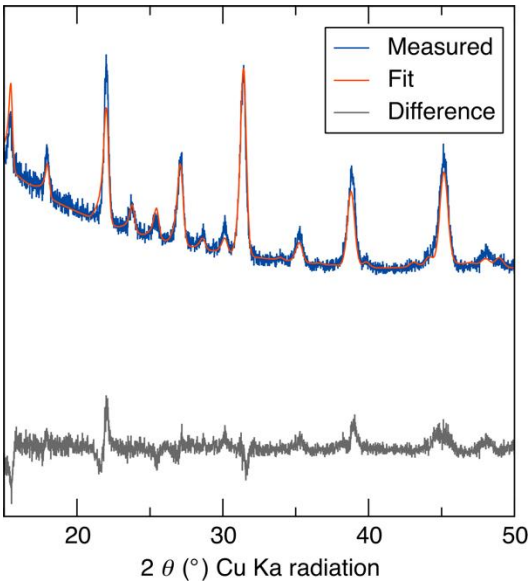

Figure S7. Rietveld refinement for compound with *x*=0.36 showing the PXRD data, the Rietveld fit produced by TOPAS, and the difference between them.

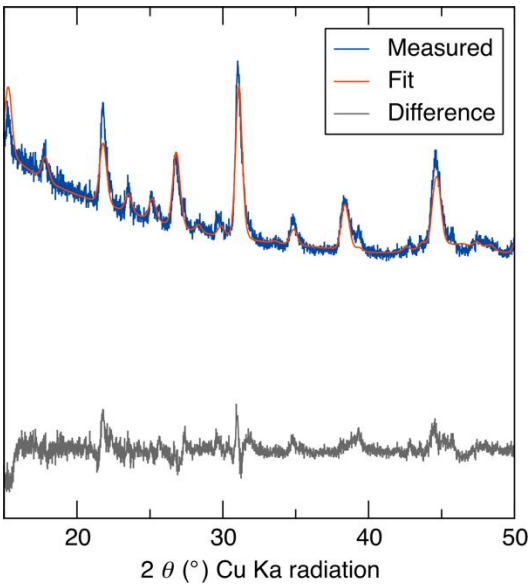

Figure S8. Rietveld refinement for compound with *x*=0.52 showing the PXRD data, the Rietveld fit produced by TOPAS, and the difference between them.

Section S3. Additional calculation data

Table S7. PBE band gaps (in eV), valence band minima and conduction band maxima for compounds simulated in the *Pm*–31 structure with lattice parameters from $Cs_3Bi_2Cl_{8.16}I_{0.84}$ single crystal diffraction. For indirect bandgaps, the smallest direct band gap is additionally listed.

Composition	w/o SOC				w/SOC			
	DBG	IBG	VBM	CBM	DBG	IBG	VBM	CBM
$Cs_3Bi_2Cl_9$	2.966	2.966	*Γ -M*	*Γ*	2.184	2.074	*Γ -M*	*A*
$Cs_3Bi_2Cl_6I_3$	2.405	2.404	*K- Γ*	*Γ*	1.487	1.413	*Γ*	*A*
$Cs_3Bi_2Cl_3I_6$	1.874	1.841	*K- Γ*	*Γ*	1.57	1.554	*K- Γ*	*Γ*
$Cs_3Bi_2I_9$	1.657	1.552	*K- Γ*	*Γ*	1.331	1.24	*K- Γ*	*A*

Table S8. PBE band gaps (in eV), valence band minima and conduction band maxima for $Cs_3Bi_2Cl_9$ simulated in the *Pnma* structure with lattice parameters from $Cs_3Bi_2Cl_9$ single crystal diffraction. For indirect bandgaps, the smallest direct band gap is additionally listed.

Composition	w/o SOC				w/SOC			
	DBG	IBG	VBM	CBM	DBG	IBG	VBM	CBM
$Cs_3Bi_2Cl_9$	2.966	2.966	*Γ -M*	*Γ*	2.184	2.074	*Γ -M*	*A*
$Cs_3Bi_2Cl_6I_3$	2.405	2.404	*K- Γ*	*Γ*	1.487	1.413	*Γ*	*A*
$Cs_3Bi_2Cl_3I_6$	1.874	1.841	*K- Γ*	*Γ*	1.57	1.554	*K- Γ*	*Γ*
$Cs_3Bi_2I_9$	1.657	1.552	*K- Γ*	*Γ*	1.331	1.24	*K- Γ*	*A*

Table S9. HSE06 band gaps (in eV), valence band minima and conduction band maxima for the compounds simulated in *Pm*–31 structures with lattice parameters from $Cs_3Bi_2Cl_{8.16}I_{0.84}$ single crystal diffraction. For indirect bandgaps, the smallest direct band gap is additionally listed.

Composition	w/SOC			
	DBG	IBG	VBM	CBM
$Cs_3Bi_2Cl_9$	2.938	2.827	*G*	*A*
$Cs_3Bi_2I_9$	1.764	1.677	*K-G*	*A*

Table S10. PBE band gaps (in eV), valence band minima and conduction band maxima for compounds simulated in hypothetical *Pm*–31 $Cs_3Bi_2Cl_{9-x}I_x$ structures with linearly-interpolated lattice parameters for iodine incorporation between 0% (x = 0) and 100% (x = 9) based on powder Rietveld diffraction trendlines. For indirect bandgaps, the smallest direct band gap is additionally listed.

0% I / 100% Cl	Composition	w/SOC			
		DBG	IBG	VBM	CBM
a = 7.68 Å	$Cs_3Bi_2Cl_9$	2.204	2.086	*Γ-M*	*A*
c = 9.46 Å	$Cs_3Bi_2Cl_6I_3$	1.473	1.395	*Γ*	*A*

	$Cs_3Bi_2Cl_3I_6$	1.530	1.507	*K-Γ*	*Γ*
	$Cs_3Bi_2I_9$	1.305	1.205	*K-Γ*	*Γ*
20% I / 80% Cl	Composition	w/SOC			
		DBG	IBG	VBM	CBM
a = 7.85 Å	$Cs_3Bi_2Cl_9$	2.155	2.053	*Γ-M*	*A*
c = 9.61 Å	$Cs_3Bi_2Cl_6I_3$	1.499	1.428	*Γ*	*A*
	$Cs_3Bi_2Cl_3I_6$	1.620	1.609	*K-Γ*	*A*
	$Cs_3Bi_2I_9$	1.366	1.271	*K-Γ*	*A*
40% I / 60% Cl	Composition	w/SOC			
		DBG	IBG	VBM	CBM
a = 8.03 Å	$Cs_3Bi_2Cl_9$	2.080	1.99	*Γ*	*A*
c = 9.77 Å	$Cs_3Bi_2Cl_6I_3$	1.501	1.435	*Γ*	*A*
	$Cs_3Bi_2Cl_3I_6$	1.672	1.63	*K-Γ*	*A*
	$Cs_3Bi_2I_9$	1.406	1.31	*K-Γ*	*A*
60% I / 40% Cl	Composition	w/SOC			
		DBG	IBG	VBM	CBM
a = 8.20 Å	$Cs_3Bi_2Cl_9$	1.979	1.899	*Γ*	*A*
c = 9.92 Å	$Cs_3Bi_2Cl_6I_3$	1.480	1.418	*Γ*	*A*
	$Cs_3Bi_2Cl_3I_6$	1.691	1.621	*Γ*	*A*
	$Cs_3Bi_2I_9$	1.424	1.329	*K-Γ*	*A*
80% I / 20% Cl	Composition	w/SOC			
		DBG	IBG	VBM	CBM
a = 8.37 Å	$Cs_3Bi_2Cl_9$	1.828	1.793	*Γ*	*A*
c = 10.07 Å	$Cs_3Bi_2Cl_6I_3$	1.439	1.381	*Γ*	*A*
	$Cs_3Bi_2Cl_3I_6$	1.680	1.587	*Γ*	*A*
	$Cs_3Bi_2I_9$	1.422	1.326	*Γ-M*	*A*
100% I / 0% Cl	Composition	w/SOC			
		DBG	IBG	VBM	CBM
a = 8.56 Å	$Cs_3Bi_2Cl_9$	1.639	*N/A*	*A*	*A*
c = 10.22 Å	$Cs_3Bi_2Cl_6I_3$	1.336	1.332	*Γ-M*	*A*
	$Cs_3Bi_2Cl_3I_6$	1.643	1.535	*Γ*	*A*
	$Cs_3Bi_2I_9$	1.352	1.301	*Γ-M*	*A*